$\mathcal{PT}$ phase transitions of edge states at $\mathcal{PT}$ symmetric interfaces in non-Hermitian topological insulators

Xiang Ni,[1,2] Daria Smirnova,[1,3,4] Alexander Poddubny,[4,5,6] Daniel Leykam,[7,*]
Yidong Chong,[7,8] and Alexander B. Khanikaev[1,2,†]

[1]*Department of Electrical Engineering, Grove School of Engineering, The City College of the City University of New York,*
140th Street and Convent Avenue, New York, New York 10031, USA
[2]*Physics program, Graduate Center of the City University of New York, New York, New York 10016, USA*
[3]*Institute of Applied Physics of the Russian Academy of Sciences, Nizhny Novgorod 603950, Russia*
[4]*Nonlinear Physics Centre, Research School of Physics and Engineering, Australian National University, Canberra, ACT 2601, Australia*
[5]*ITMO University, St. Petersburg 197101, Russia*
[6]*Ioffe Institute, St. Petersburg 194021, Russia*
[7]*Division of Physics and Applied Physics, School of Physical and Mathematical Sciences, Nanyang Technological University,*
Singapore 637371, Singapore
[8]*Centre for Disruptive Photonic Technologies, Nanyang Technological University, Singapore 637371, Singapore*

We demonstrate that the parity-time ($\mathcal{PT}$) symmetric interfaces formed between non-Hermitian amplifying ("gainy") and lossy topological crystals exhibit $\mathcal{PT}$ phase transitions separating phases of lossless and decaying/amplifying topological edge transport. The spectrum of these interface states exhibits *exceptional points* (EPs) separating (i) a $\mathcal{PT}$ symmetric real-valued regime with an evenly distributed wave function in both gainy and lossy domains and (ii) a $\mathcal{PT}$ broken complex-valued regime, in which edge states asymmetrically localize in one of the domains. Despite its complex-valued character, the edge spectrum remains gapless and connects complex-valued bulk bands through the EPs. We find that the regimes exist when the real edge spectrum is embedded into the bulk continuum without mixing, indicating that the edge states are protected against leakage into the bulk by the $\mathcal{PT}$ symmetry. Two exemplary $\mathcal{PT}$ symmetric systems, exhibiting valley and Chern topological phases, respectively, are investigated and the connection with the corresponding Hermitian systems is established. Interestingly, despite the complex bulk spectrum of the Chern insulator, the bulk-interface correspondence principle still holds, as long as the topological gap remains open. The proposed systems are experimentally feasible in photonics, which is evidenced by our rigorous full-wave simulations of $\mathcal{PT}$ symmetric silicon-based photonic graphene.

I. INTRODUCTION

The unique characteristics of surface states emerging at the boundaries of topological materials have led to a huge recent interest in topological phases of solid matter [1–7], photonics [8–15], and mechanical systems [16–19]. While the most common edge configuration encountered in condensed matter physics is the free boundary of the topological materials, in classical systems, photonics in particular, the other kind of topological interfaces, commonly referred to as domain walls consisting of two topologically distinct domains, can be easily created and can be advantageous over the free boundary [9]. In particular, the shape of domain walls, defining the path of the edge states, can be reconfigurable [14,20]. As we show in this letter, introduction of an additional parity-time symmetry of domain walls can further enrich physics of topological sys-

tems, giving rise to a fundamentally different properties of the surface states compared to the free boundary configuration.

Symmetries of interfaces in topological materials defined by the direction of a cut are known to have a direct impact on surface states. For systems with topological properties emerging from spatial symmetries, such as crystalline topological insulators, respecting of the essential symmetries at interfaces is determining for the very existence of topological surface states [21]. In the case of domain walls formed between crystals of commensurate lattice structure the interfaces can possess even higher symmetry [22], i.e., they can obey inversion and glide symmetries, which are absent in the case of free-standing edges and surfaces. These additional symmetries, in their turn, define the symmetry of the wave function of the topological surface states supported by the domain wall. As an example, the reversal of a synthetic gauge field represents one of the most common topological domain walls in photonics [9,14]. In this case, the topological invariant, i.e., Chern or spin-Chern number, in two adjacent domains has the same magnitude, but reverses its sign across the domain wall, leading to the doubling of the number of edge states compared to the case of free-standing boundaries of the same

---

*Present address: Center for Theoretical Physics of Complex Systems, Institute for Basic Science, Daejeon 34126, Republic of Korea.
†akhanikaev@ccny.cuny.edu

crystals. Due to the presence of inversion symmetry across the interfaces, the edge states confined to the domain wall can be immediately classified as odd or even with respect to this symmetry. Interestingly, any reduction of the domain wall symmetry, i.e., change of its direction, leads to cross-scattering between these states, but does not affect their chiral or helical character, and the backscattering remains inhibited. This simple example shows that the symmetry of the domain walls can be exploited to control the distribution of energy between multiple surface states, which can be utilized to selectively steer electromagnetic states in multiplexed topological photonic systems [20,23,24].

In this article, by considering non-Hermitian parity-time-symmetric ($\mathcal{PT}$) Hamiltonians [25,26], we show that the domain wall geometry allows one to expand the role of interface symmetries even further. While non-Hermitian topological systems have recently attracted a great deal of attention, it was suggested that non-Hermitian potentials alone cannot yield new topological phases [27]. On the other hand, the effect of $\mathcal{PT}$ symmetric potentials on topological edge states is the most fascinating theoretical questions being explored in recent publications [28–37].

Whereas the combination of Hermitian topology and non-Hermitian perturbing potentials may have some interesting impact on the bulk spectrum leading to topological phase transitions [28–37], fundamentally new concepts are required to account for the non-Hermiticity in topological systems. The domain walls offer a natural way to consider the role of non-Hermiticity in a context of $\mathcal{PT}$ symmetry; assuming an interface between topologically distinct crystals with gain and loss, one enables a new configuration of $\mathcal{PT}$ symmetric domain walls. Whereas the bulk states of such two crystals separately are expected to be complex valued, one can argue that the $\mathcal{PT}$ symmetry of the domain wall formed between them may still warrant a real spectrum of the surface states [38–41], at least in some range of values of gain/loss and wave number.

Another intriguing question is how the bulk-interface correspondence principle will apply to such a system with a complex-valued bulk spectrum, and whether the edge spectrum will adapt to interconnect such bulk bands and in what form. Here, we discover that despite the non-Hermiticity, the bulk-interface correspondence holds in a wide range of gain/loss, but the edge spectrum exhibits a transition from a $\mathcal{PT}$ preserved phase to spontaneously $\mathcal{PT}$ broken phase. In the case of $\mathcal{PT}$ preserved phase, the wave function of the edge state is evenly distributed between gainy and lossy domains, leading to the formation of $\mathcal{PT}$ symmetric edge states with real spectrum. In the second case, the $\mathcal{PT}$ symmetry of edge states is spontaneously broken, and their wave function is asymmetrically distributed over the two domains, resulting in a complex edge spectrum. The transition between two phases is separated by EPs where the edge states coalesce [42–44]. Nonetheless, the number of the edge states is preserved across such a $\mathcal{PT}$-transition, and the edge spectrum interconnects complex bulk bands along the imaginary energy direction. Recent successes in experimental realization of non-Hermitian topological photonic systems make us believe that $\mathcal{PT}$ symmetric domain walls may lead to a variety of novel approaches to actively control robust guiding, lasing, and nonlinear opti-

cal effects, thus further expanding the toolkit of topological photonics [45–47].

Below we present a set of thorough analytical and numerical studies of several two-dimensional (2D) models of $\mathcal{PT}$ symmetric domain walls separating non-Hermitian honeycomb lattices with gain and loss. The paper is organized as follows. First, we show that for a valley-Hall-like lattice, there exist real-energy edge states that form loops in the complex energy diagram, bridging the two valleys of the Brillouin zone. In the limiting case of vanishing gain and loss, these "$\mathcal{PT}$ edge states" reduce to conventional valley edge states (Sec. II). They are sensitive to the local domain wall symmetry, but robust to the strength of the gain and loss for the case of a locally parity-symmetric wall. Next, the interplay of non-Hermiticity and topology with broken time reversal (TR) symmetry in the context of a non-Hermitian variant of the Haldane model with and without $\mathcal{PT}$ symmetric interface is analyzed (Sec. III) and nonreciprocal $\mathcal{PT}$ edge states located at the $\mathcal{PT}$ symmetric interface are observed. To test our analytic predictions in experimentally feasible context, an optical analogue of graphene with and without $\mathcal{PT}$ symmetric interface is studied both by rigorous full-wave simulations and within the analytical continuous $\boldsymbol{k} \cdot \boldsymbol{p}$-type plane-wave approximation (Sec. IV).

II. BRIDGING VALLEYS BY $\mathcal{PT}$ SYMMETRIC PHASE

We first consider a 2D honeycomb valley-Hall lattice model shown in Fig. 1. The lattice consists of two domains, with gain (loss) for site A (B) in the upper domain II and loss (gain) for site B (A) in the lower domain I. The structure has a strip geometry: it is periodic along the x direction, parallel to the interface, and has a finite width $2(N+1)a_0$ along the y direction with zigzag cut at the ends, where a_0 is the lattice constant. Onsite perturbed potentials are also introduced for site A (B) in domain I and site B (A) in the domain II, as shown in Fig. 1(a) [Fig. 1(b)]. The lattices with bearded cut and armchair cut at the $\mathcal{PT}$ interface have the same orientation of the strip as that of zigzag cut, in Figs. 1(c) and 1(d). Equations of motion are derived from the following tight binding model (TBM) (for details, refer to Ref. [48]):

$$\epsilon \psi_{I,A}(n) = -\psi_{I,B}(n+1) - g_k \psi_{I,B}(n) - \Pi m \psi_{I,A}(n),$$
$$n = 0, 1, 2, \ldots, N-1,$$
$$\epsilon \psi_{I,B}(n) = -\psi_{I,A}(n-1) - g_k \psi_{I,A}(n) - \Pi_0 m \psi_{I,B}(n),$$
$$n = 1, 2, \ldots, N;$$
$$\epsilon \psi_{II,A}(n) = -\psi_{II,B}(n-1) - g_k \psi_{II,B}(n) - \Pi_0 m^* \psi_{I,A}(n),$$
$$n = 1, 2, \ldots, N,$$
$$\epsilon \psi_{II,B}(n) = -\psi_{II,A}(n+1) - g_k \psi_{II,A}(n) - \Pi m^* \psi_{II,B}(n),$$
$$n = 0, 1, 2, \ldots, N-1. \tag{1}$$

Here, $g_k = 2\cos(k_x/2)$, k_x is the momentum vector along the x direction, $\psi_{s,j}(n)$ is the component of the wave function within the domain $s = I, II$ at site (n, j), $j = A, B$. $m = m_r + im_i$, m_r, and m_i are the real and imaginary part of perturbing onsite potential, respectively. For the sake of generality, we consider two cases that are both
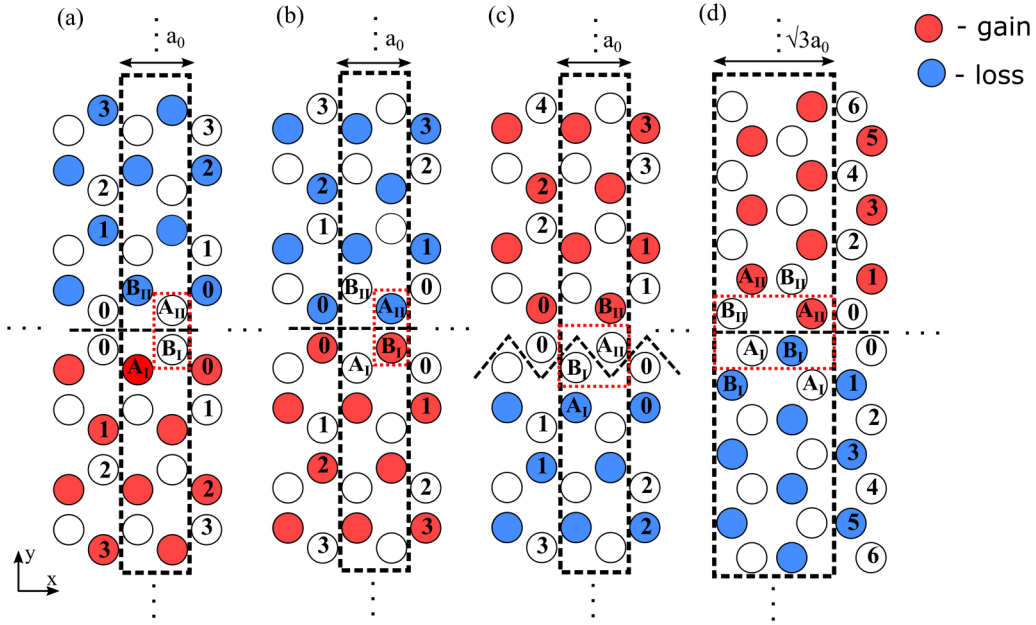
FIG. 1. Different types of $\mathcal{PT}$ symmetric interfaces (valley-Hall domain wall), with different local symmetry of the wall (see the red-dashed rectangle). (a) Zigzag cut with real (locally parity preserved) domain wall. (b) Zigzag cut with imaginary (locally parity broken) domain wall. (c) Bearded cut with real domain wall. (d) Armchair cut with real left part of domain wall and imaginary right part of the domain wall.

$\mathcal{PT}$ symmetric but differ by the microscopic structure of the interface between the domains. We call these configurations "locally P-symmetric" and "locally P-broken" domain walls, and they are shown in Figs. 1(a) and 1(b), respectively. In the first case, $\Pi = 1$, $\Pi_0 = 0$, the local parity of the sites at the boundary [red rectangle in Fig. 1(a)] is preserved, and the on-site energies adjacent to the wall are real. In the second case, $\Pi = 0$, $\Pi_0 = 1$, the local parity at the boundary is broken, while the adjacent on-site energies are imaginary. Globally, both domain wall configurations are $\mathcal{PT}$ symmetric. At the domain wall, the TBM equations are

$$\epsilon\psi_{I,B}(0) = -\psi_{II,A}(0) - g_k\psi_{I,A}(0) - \Pi_0 m\psi_{I,B}(0),$$
$$\epsilon\psi_{II,A}(0) = -\psi_{I,B}(0) - g_k\psi_{II,B}(0) - \Pi_0 m^*\psi_{I,A}(0), \quad (2)$$

while at the outer boundaries of the strip,

$$\epsilon\psi_{I,A}(n) = -\psi_{II,B}(n) - g_k\psi_{I,B}(n) - \Pi m\psi_{I,A}(n),$$
$$\epsilon\psi_{II,B}(n) = -\psi_{II,A}(n) - g_k\psi_{II,A}(n) - \Pi m^*\psi_{II,B}(n). \quad (3)$$

In Fig. 2, we show the effect of gain and loss on the complex band structure. The complex energies are calculated from Eqs. (1)–(3) for different values of gain/loss parameter m_i but the same $m_r = 0.3$. Real-valued energies of discrete edge states are found for both locally P-symmetric and P-broken domain walls, and shown in Figs. 2(a) and 2(b) by thick blue and red lines, respectively. In the case when m_r is much larger than m_i, shown in Fig. 2(a), these lossless edge states look much like the conventional valley edge states. Four edge states are embedded into the bulk spectrum and are continuous along k_x. If m_i is increased and becomes comparable with m_r [$m_i = m_r = 0.3$ in Fig. 2(b)], the dispersion curves of the edge bands form two heart-shaped loops which are different

in size. The edge states for the large loop correspond to the locally P-symmetric domain wall, while those for the small loop correspond to the locally P-broken domain wall. If m_i becomes much larger than m_r, the smaller loop shrinks and eventually vanishes, while the larger loop persists [Fig. 2(c)]. Lossless edge states for the locally P-symmetric domain wall
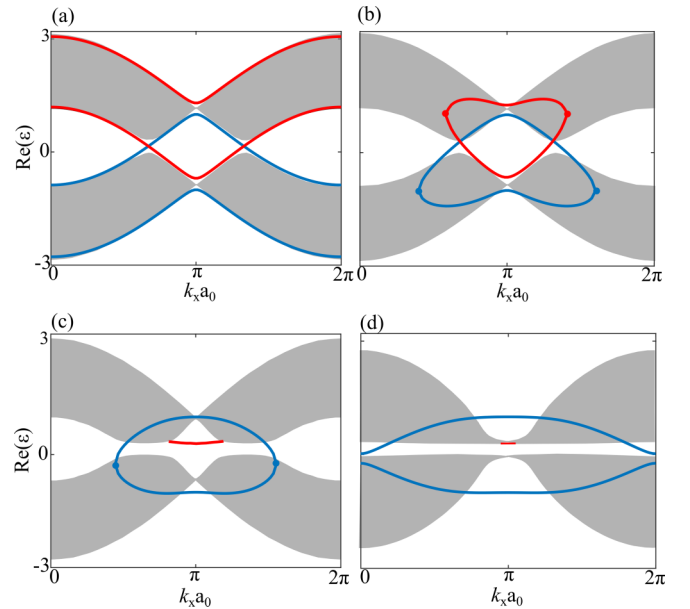

FIG. 2. Energy spectra (grey color) calculated from the TBM and edge states found analytically for locally P-symmetric (blue) and locally P-broken (red) zigzag domain walls. The parameters are (a) $m_r = 0.3$, $m_i = 0.05$. (b) $m_r = 0.3$, $m_i = 0.3$. (c) $m_r = 0.3$, $m_i = 1.2$. (d) $m_r = 0.3$, $m_i = 3$. The number of cells for each domain is $N = 50$.
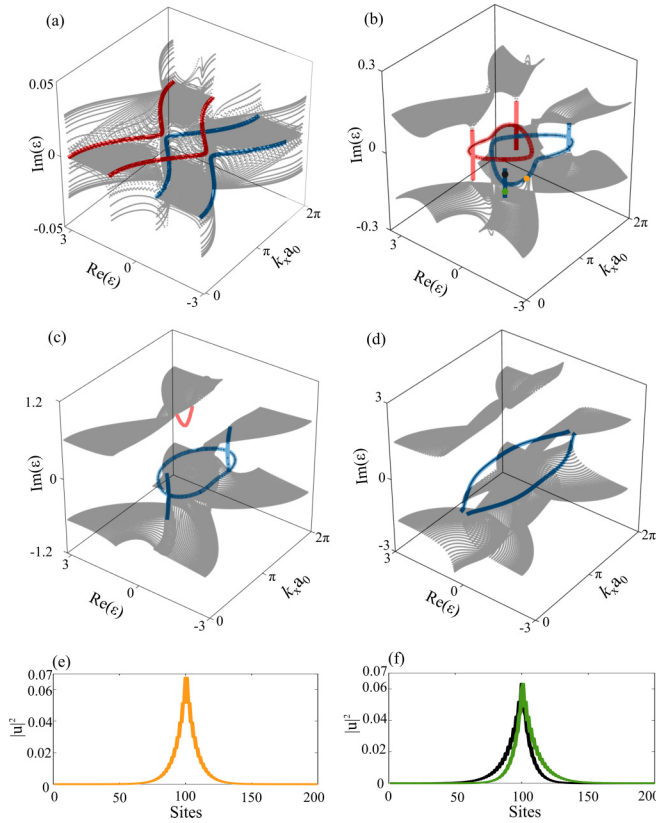
FIG. 3. Complex band structure of the same cases in (a)–(d) as the ones in Fig. 2. The wave function profiles of (e) $\mathcal{PT}$ edge states indicated by an orange dot in (b) and (f) complex-valued edge states with complex conjugated pairs indicated by black and green dots in (b) are schematically presented.

survive even for very strong gain/loss. Interestingly, we see in Fig. 2(d) that when m_i is large enough to split the loop bands into separate bands, the lossless edge bands persist, embedded within the bulk continuum.

It is interesting to take a closer look at the band structures in the 3D complex space. Figure 3 demonstrates the same cases as ones in Fig. 2, with the imaginary part of energies being plotted in the third dimension. Because of the $\mathcal{PT}$ symmetry of the Hamiltonian, the complex bulk bands have inversion symmetry with respect to the $\epsilon_i = 0$ plane. When m_i is small compared to m_r, both the edge states and a few bulk states have real energies. If the magnitude of m_i increases, these bulk states undergo a $\mathcal{PT}$-breaking transition and split into complex conjugated pairs [Figs. 3(b)–3(d)], and there are two regimes describing the behaviors of the edge states. In the first regime in Figs. 3(b)–3(d), edge dispersion curves are real-valued lying in the $\epsilon_i = 0$ plane, and their wave functions are distributed evenly along the domain wall, as shown in Fig. 3(e). In the second regime in Figs. 3(b) and 3(c), however, the wave functions of edge states with the complex-valued energies become unevenly distributed among the domains across the domain wall, and this asymmetry increases as one moves farther away from the EPs. The edge states with energies above and below the $\epsilon_i = 0$ plane are complex conjugated partners [for example, the black and green dots in Fig. 3(b)], and their respective wave functions are symmetric to each

other [in Fig. 3(f)]. The two scenarios are connected by exceptional points (EPs), where multiple (usually two) eigenvalues and their associated eigenstates coalesce, and the Hamiltonian becomes defective [42,43]. For a zigzag cut, the edge curves in the second regime will disappear if the magnitude of m_i is too small or too large, as shown in Figs. 3(a) and 3(d). In the following text we study these peculiar behaviors of the edge states with a nonperturbative analytical method.

III. $\mathcal{PT}$ EDGE STATES

Next, we derive analytic descriptions for the real-energy edge states in the first regime preserving the $\mathcal{PT}$ phase, which we will henceforth refer to as "$\mathcal{PT}$ edge states." We start from the equations of motion (1,2). The stripe is considered finite, which formally implies the following boundary conditions at the external boundaries of the stripe

$$\psi_{I/II,B/A}(n+1) = 0. \tag{4}$$

Clearly, for $N \to \infty$, any edge states localized at the ends of the stripe barely feel the effects of gain/loss in the other domain; therefore, they possess complex energies with imaginary parts equal to the magnitude of the gain/loss in their respective domains. Here, we focus on the edge states confined to the central domain wall, whose properties are inherently related to the $\mathcal{PT}$ symmetric configuration of the structure.

We observe that the Hamiltonian constructed from Eqs. (1), (2), and (4) remains invariant under the action of $\mathcal{PT}$ symmetry operator defined upon the wave functions as

$$\mathcal{PT}\psi(y) = \psi^*(-y). \tag{5}$$

Consequently, if the eigenstates of the Hamiltonian are simultaneously the eigenstates of the $\mathcal{PT}$ symmetry operator, different from the Hermitian case, the antiunitary operator follows

$$\mathcal{PT}\psi(y) = e^{-i\varphi}\psi(y), \tag{6}$$

where $e^{-i\varphi}$ is the eigenvalue of the $\mathcal{PT}$ operator, then the eigenvalues of Hamiltonian corresponding to such eigenstates are real; these states possess the specific symmetry. If the $\mathcal{PT}$ symmetric phase is spontaneously broken by tuning the Hamiltonian parameters, the energy eigenvalues are divided into complex conjugate pairs after their states coalesce at the EPs [44] (but still merge with bulk continuum). Both extended and localized states may or may not have $\mathcal{PT}$ symmetry phase, and the $\mathcal{PT}$ symmetry phase is broken for all extended states if the gain/loss is tuned to be large.

Based on Eqs. (5) and (6), the wave function components in the two domains should be related as

$$\psi_{I,A/B}(n) = e^{i\varphi}\psi_{II,B/A}^*(n). \tag{7}$$

Thereby, we recover the relation

$$e^{-i\beta} = \frac{\psi_{e,I,A}(n)}{\psi_{e,I,B}(n+1)} = \frac{\psi_{e,II,B}^*(n)}{\psi_{e,II,A}^*(n+1)}$$

$$= \frac{\psi_{e,II,A}(0)}{\psi_{e,I,B}(0)} = \frac{\psi_{e,I,B}^*(0)}{\psi_{e,II,A}^*(0)}, \tag{8}$$
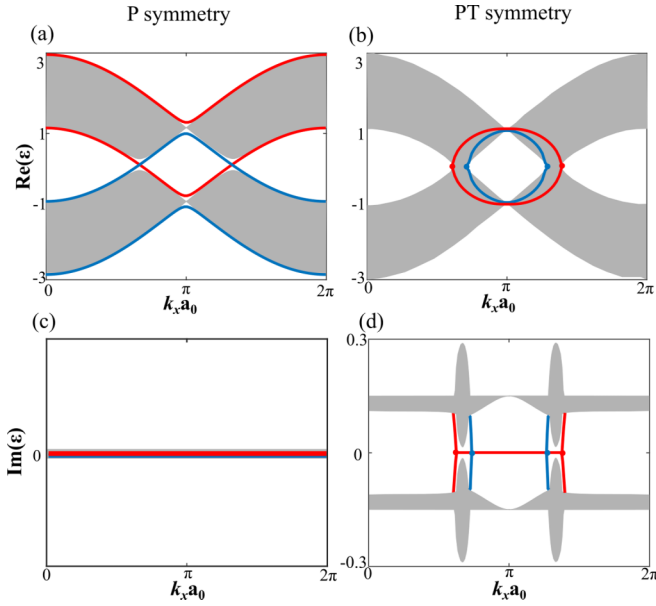
FIG. 4. Comparison of real [(a) and (b)] and imaginary [(c) and (d)] energy dispersions for two extreme cases, namely, valley edge states with $m_r = 0.3$ and $m_i = 0$ [(a) and (c)] and $\mathcal{PT}$ edge states with $m_r = 0$ and $m_i = 0.3$ [(b) and (c)]. Grey shaded regions represent the bulk bands, red and blue lines correspond to the edge states at locally P-broken and P-symmetric interfaces, and the solid dots are the EPs. The number of cells employed in the tight-binding method for each domain is $N = 50$.
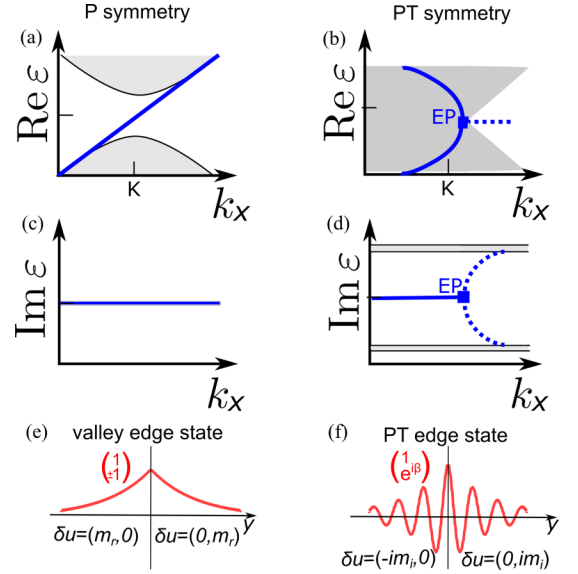

FIG. 5. Same as Fig. 4, but in the $\mathbf{k} \cdot \mathbf{p}$ approximation near the Dirac point. (a)–(d) illustrate schematics of two extreme cases, namely, valley edge states with $m_i = 0$ and $\mathcal{PT}$ edge states with $m_r = 0$ [(b) and (d)]. Dispersion of real [(a) and (b)] and imaginary [(c) and (d)] parts of the complex energies are shown by shaded areas and blue curves for bulk continuum states and $\mathcal{PT}$ edge states, respectively. [(e) and (f)] Profiles of the real parts of the envelope wave function of interface states. Bloch function structure and the on-site potential δu for each domain are indicated.

where we have introduced another phase factor $\beta = \varphi - 2 \arg(\psi_{e,II,A}(0))$. Equations (8) equivalently yield

$$\psi_{e,I,A}(n) = e^{-i\beta} \psi_{e,I,B}(n+1)$$

$$\psi_{e,II,A}(n+1) = e^{-i\beta} \psi_{e,II,B}(n), \tag{9}$$

$$n = 0, 1, \ldots, N-1.$$

The edge states satisfying Eq. (7) belong to the $\mathcal{PT}$ symmetric phase, and the corresponding energy spectra are real. The $\mathcal{PT}$ edge states are supposed to be localized at the domain wall; moreover, they are concentrated at sites $(0, B)$ in domain I and sites $(0, A)$ in domain II.

Thus, the solutions for the edge states assume the Bloch form

$$\psi_{e,I,A}(n) = a_I e^{ik_{y,I}(n+1)}, \quad \psi_{e,II,A}(n) = a_{II} e^{ik_{y,II}n},$$

$$\psi_{e,I,B}(n) = b_I e^{ik_{y,I}n}, \quad \psi_{e,II,B}(n) = b_{II} e^{ik_{y,II}(n+1)}, \tag{10}$$

$$n = 0, 1, \ldots, N-1,$$

where, due to the $\mathcal{PT}$ symmetry condition (7), the wave vectors and Bloch function amplitudes are related as $k_{y,I} = -k_{y,II}^* = p + i\kappa$, $a_I = e^{i\varphi} b_{II}^*$, and $b_I = e^{i\varphi} a_{II}^*$. The parameter κ^{-1} characterizes the decay length away from the interface. Remarkably, utilizing the Bloch ansatz (10) in Eq. (8) with the boundary equations (2) and (3), we get the continuity condition for the Bloch vector components $a_I = a_{II}$, $b_I = b_{II}$, being of the same absolute value:

$$\frac{a_I}{b_I^*} = \frac{a_{II}}{b_{II}^*} = \frac{a_I}{b_{II}^*} = \frac{b_I}{a_{II}^*} = e^{i\varphi}.$$

Substituting Eq. (10) into Eq. (1), we then obtain

$$\begin{bmatrix} (\epsilon_e + m + e^{i\beta})e^{-ik_{y,I}} & g_k \\ g_k & (\epsilon_e + e^{-i\beta})e^{ik_{y,I}} \end{bmatrix} u_e = 0, \tag{11}$$

where $u_e = [a_I, b_I]^T$. Solving the secular equation (11) and separating the real and imaginary parts, we get two equations, which define the dispersion of $\mathcal{PT}$ edge states,

$$m_i(\epsilon_e + \cos(\beta)) + m_r \sin(\beta) = 0,$$

$$(\epsilon_e + m_r)\epsilon_e + 2\cos(\beta)\epsilon_e + m_r \cos(\beta)$$
$$- m_i \sin(\beta) - g_k^2 + 1 = 0. \tag{12}$$

Alternatively, denoting the ratio of real and imaginary parts of the mass term $r = m_r / m_i$, we rewrite Eq. (12) as

$$(r^2 - 1)\epsilon_e^2 + (1 + r^2)m_r \epsilon_e - (1 + r^2)(g_k^2 - 1)$$

$$= \pm(2r\epsilon_e + m_r(r + r^{-1}))\sqrt{-\epsilon_e^2 + r^2 + 1}. \tag{13}$$

The analytically derived dispersion of the edge modes perfectly agrees with the numerical tight-binding calculations.

Remarkably, the parity symmetry with respect to the interface is restored if no gain/loss is present at the lattice sites, i.e., $m_i = 0$. Consequently, the phase difference may take two values $\beta = 0, \pi$, which clearly correspond to the symmetric and anti-symmetric wave functions of the Hermitian valley edge states, respectively [49]. Therefore the *valley edge states* of the Hermitian model can be regarded as special cases of the $\mathcal{PT}$ symmetric edge states analyzed above. We will now compare the representative cases of $m_i = 0$ and $m_r = 0$ in more detail. Figure 4 presents the tight-binding calculations

for these two cases in the whole Brillouin zone. Figure 5 schematically shows the results of the $\boldsymbol{k} \cdot \boldsymbol{p}$ approximation in the vicinity of the Dirac points for the case of a locally P-symmetric domain wall (for details, see Supplemental Material III Ref. [48]). The calculation demonstrates that both

$$\epsilon_e = \begin{cases} \pm 1 - \frac{m_r - \sqrt{m_r^2 + 4g_k^2}}{2}, & \text{locally P} - \text{symmetric domain wall,} \\ \pm 1 - \frac{m_r + \sqrt{m_r^2 + 4g_k^2}}{2}, & \text{locally P} - \text{broken domain wall.} \end{cases} \tag{14}$$

Four valley edge states located at the locally P-symmetric (red bands) and locally P-broken (blue bands) domain walls are found, among which two bands with parity $+1$ (symmetric wave function along the interface) cross the band gap and another two with parity -1 (antisymmetric wave function along the interface) lie at the edges of the bulk spectrum, as seen in Fig. 4(a). From Eq. (14), it follows that at $k = \pi$ the valley edge states have energy $\epsilon_e = \pm 1$ for the locally P-symmetric domain wall, which is a general property of the $\mathcal{PT}$ edge states. Near the Dirac points, the valley edge states have the well-known linear dispersion [blue line in Fig. 5(a)]

$$\epsilon_e = \frac{-m_r}{2} \pm vk \tag{15}$$

traversing the gap between the Dirac cones of bulk states [shaded areas in Fig. 5(a)]. Here, $k = k_x - \pi \mp \frac{\pi}{3}$ is the detuning of the wave vector from the Dirac point, $v = \frac{\sqrt{3}}{2}$ is the Fermi velocity, and we assume that m_r is small. These valley edge states are associated with the valley Hall effect [50], and they can be gapped from bulk states by increasing the magnitude of m_r.

In contrast to the valley edge states, which have been widely explored in the literature, the edge states located at the $\mathcal{PT}$ symmetric interface appearing solely due to m_i have not been studied thus far. Though the real bulk spectra are not gapped, the imaginary parts of the bulk bands are discontinuous at 0, and the $\mathcal{PT}$ edge bands in the first regime stay within the plane $\text{Im}(\epsilon_e) = 0$ and connect with the bulk bands through parabolic edge bands in the second regime, as indicated by solid dots in Figs. 4(b) and 4(d) as long as $m_i \leqslant 3$. There is no connection between the $\mathcal{PT}$ edge bands and the bulk bands if $m_i > 3$, as will be shown in the following section from the analysis of EPs in Fig. 6(a). The energies of the $\mathcal{PT}$ edge states can be expressed in the compact form

$$\epsilon_e = \pm \sqrt{1 - t},$$
$$t = \frac{2g_k^2 + m_i^2 \pm \sqrt{\left(2g_k^2 + m_i^2\right)^2 - 4g_k^4}}{2}, \tag{16}$$

where the $\pm$ signs in t correspond to the points in the large and small loops, for locally P-symmetric and locally P-broken cases, respectively. The spectra of the edge states when $m_i = 0.3$ are plotted in red and blue color in Figs. 4(b) and 4(d). They form two loops and exactly reproduce the numerical tight-binding calculations. The analysis of the $\mathcal{PT}$ symmetric case with $m_r = 0$, $|m_i| \ll 1$ near the Dirac point is presented in Figs. 5(b) and 5(d). Both the tight-binding calculation

these cases inherit the general characteristics of lossless edge states, with the gap either in real [$m_i = 0$, panels (a) and (c) of Figs. 4 and 5] or imaginary [$m_r = 0$, panels (b) and (d)] part of the bulk spectrum crossed by the edge states.

In particular, for $m_i = 0$, Eq. (12) yields the solutions in Fig. 4(d), and $\boldsymbol{k} \cdot \boldsymbol{p}$ results in Fig. 5(d), show that the imaginary part of the complex bulk spectrum has a gap of width m_i, which is traversed by the parabolic dispersion of edge states

$$\epsilon_e^2 = m_i \pm 2vk. \tag{17}$$

It demonstrates that the presence of the lossless edge states does not require a gap in the real bulk bands, allowing these edge states to be embedded in the continuum of bulk modes. The spectrum changes dramatically at the EPs $k = \mp m_i/(2v)$, where the gap in the real part of the bulk spectrum vanishes and the edge states exhibit the $\mathcal{PT}$ phase transition from complex energy (dotted blue curves in Fig. 5) to real energy (solid blue curves). Interestingly, the group velocity corresponding to the dispersion law (17) diverges at the EPs, although the concept of group velocity should be used with care in the context of non-Hermitian system [51].

In order to further elucidate the difference between the P-symmetric and $\mathcal{PT}$ symmetric interface states, we plot in
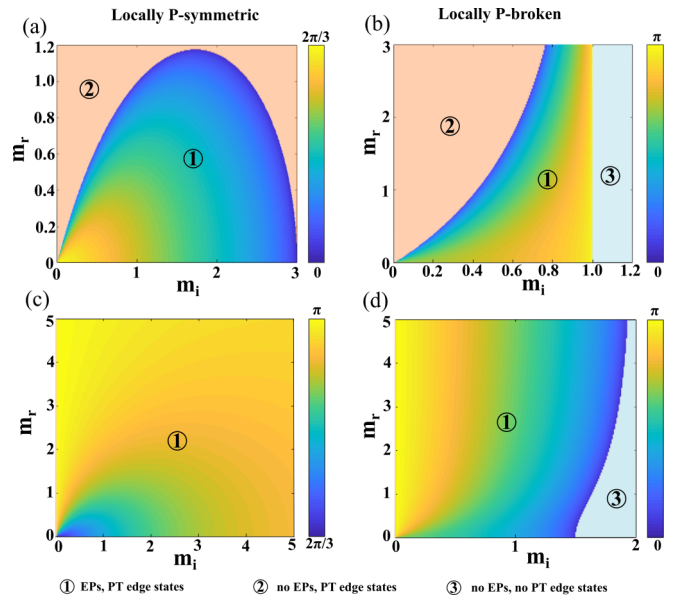

FIG. 6. Variation of the EPs' position in the Brillouin zone obtained from Eqs. (21) and (22) depending on m_i and m_r for (a) zigzag cut and a locally P-symmetric domain wall, (b) zigzag cut and locally P-broken domain wall, (c) bearded cut and locally P-symmetric, and (d) bearded cut and locally P-broken domain wall. EPs do not exist in light red and blue shaded regions, $\mathcal{PT}$ edge states are present in the light red region, but not in the light blue region.

Figs. 5(e) and 5(f) the wave functions of interface states in the $\mathbf{k} \cdot \mathbf{p}$ model. The wave functions satisfy the general symmetry considerations established in Eqs. (8) and (9). Namely, for valley states, the wave function envelope is real and monotonically decays from the interface, while the corresponding Bloch function has a certain parity, $\beta = 0, \pi$. For $\mathcal{PT}$ edge states the envelope function exhibits damped oscillations with distance y from the interface $\propto \exp(ipy - \kappa|y|)$, as shown in Fig. 5(f).

IV. EFFECT OF LOCAL SYMMETRY AT THE DOMAIN WALL

Here we examine the effect of the different domain terminations on the existence of edge states. We stress that although equations (13) fully recover the edge state energies, they are obtained without explicit use of the boundary conditions (2) and (3) and rely only on the assumption of $\mathcal{PT}$ symmetry. Additional insights about the edge states can be drawn from the *local* P-symmetry of the $\mathcal{PT}$ symmetric domain wall, which is preserved in Fig. 1(a) and broken in Fig. 1(b). Since $g(k_x = \pi) = 0$, it follows from Eq. (1) that the $\mathcal{PT}$ edge states at $k_x = \pi$ residing at the domain wall are completely decoupled from the nearest neighbors. This suggests a short decay length $\kappa^{-1} \ll 1$ at $k_x = \pi$, which is verified by the numerical calculation in Fig. S1(a) Ref. [48]. Consequently, these strongly localized $\mathcal{PT}$ edge states only "see" the local wall symmetry in the red dashed region. The wall in Fig. 1(a) is locally parity-symmetric, and thus the $\mathcal{PT}$ edge states can be assigned a certain parity, and their energies derived from Eq. (13) are always equal to $\epsilon_e = \pm 1$ at $k_x = \pi$ no matter what the ratio $r = m_r/m_i$ is. In Fig. 1(b), the parity symmetry for the wall is broken (while the global $\mathcal{PT}$ symmetry is still preserved). Consequently, the $\mathcal{PT}$ edge states do not necessarily have a certain parity. The existence of an edge state with energy ϵ_e depends on the magnitude

of r and m_i, and the $\mathcal{PT}$ edge states vanish if m_i is too large. For example, when $r = 0$, $\epsilon_e = \pm\sqrt{1 - \sin(\beta)m_i}$, and if $m_i > \sin(\beta)^{-1}$, ϵ_e becomes complex, which contradicts the precondition of $\mathcal{PT}$ edge states, so the $\mathcal{PT}$ edge states do not exist, only complex-conjugated pairs of edge states appear inside the band gap.

With the distinct properties of $\mathcal{PT}$ edge states for different domain walls explored, we can easily distinguish the edge states corresponding to the large loop, which are localized at a locally P-symmetric domain wall, from those corresponding to the small loops, which are localized at a locally P-broken wall for specific parameters (m_i, m_r). The decay length κ^{-1} of the $\mathcal{PT}$ edge states is calculated from the conditions (2) combined with the solutions for different configurations, and is extensively discussed in Ref. [48].

V. EXCEPTIONAL POINTS

The case $\beta = \pm\frac{\pi}{2}$ is examined in detail here. Since the Hamiltonian is non-Hermitian, $H \neq H^\dagger$, the right eigenstate $|\psi_e^R(k)\rangle$ and the left eigenstate $|\psi_e^L(k)\rangle$ have to be defined separately to satisfy the eigenvalue equations

$$H(k)\big|\psi_e^R(k)\big\rangle = \epsilon_e\big|\psi_e^R(k)\big\rangle,$$
$$H^\dagger(k)\big|\psi_e^L(k)\big\rangle = \epsilon_e\big|\psi_e^L(k)\big\rangle, \qquad (18)$$

where ϵ_e is the eigenenergy of the lossless edge states in the first regime, which is real. The eigenstates $|\psi_e^{R/L}(k)\rangle$ are given explicitly by

$$\big|\psi_e^{R/L}(k)\big\rangle = \sum_{s,n,j} \psi_{e,s,j}(n)\big|u_{s,j,n}^{R/L}(k)\big\rangle, \quad n = 0, 1, \ldots, N.$$
$$(19)$$

Using the normalization condition $\langle u_i^L(k)|u_j^R(k)\rangle = \delta_{ij}$ [52], and the fact that the vectors $(|u_j^R(k)\rangle, |u_j^L(k)\rangle)$ form a complete basis in the Hilbert space (dual space), the norm of the edge eigenstates is

$$\big\langle \psi_e^L(k)\big|\psi_e^R(k)\big\rangle = \sum_n (e^{i2\beta} + 1)(|\psi_{e,I,A}(n)|^2 + |\psi_{e,I,B}(n)|^2), \quad n = 0, 1, \ldots, N. \qquad (20)$$

Here, we have exploited the $\mathcal{PT}$ symmetry condition Eq. (7) and the phase factor β defined in Eq. (8). Therefore, if $e^{i\beta} = \pm i$, then $\langle \psi_e^L(k)|\psi_e^R(k)\rangle = 0$. The vanishing of the norm indicates that the eigenstates are no longer linearly independent, while having the same eigenvalues. This is the condition for an EP, which is distinct from the case of a band degeneracy [44]. Therefore the two dispersion curves of $\mathcal{PT}$ edge states coalesce at EPs when $\beta = \pm\frac{\pi}{2}$, with the $\mathcal{PT}$ symmetric phase being spontaneously broken.

Now, we examine the dependence of the position of EPs on the gain/loss parameter m_i based on the discussion above. From Eq. (12) one finds that $\epsilon_e = \pm r$ if $\beta = \pm\frac{\pi}{2}$. Since the EPs of the $\mathcal{PT}$ edge states cannot be at $k_x = \pi$, we obtain $\beta = -\frac{\pi}{2}$ for locally P-symmetric domain wall, and $\beta = \frac{\pi}{2}$ for locally P-broken domain walls, thus

$$g_k = \begin{cases} \pm\sqrt{(r^2 + 1)(m_i + 1)}, & \text{locally P} - \text{symmetric domain wall}; \\ \pm\sqrt{(r^2 + 1)(1 - m_i)}, & \text{locally P} - \text{broken domain wall}. \end{cases} \qquad (21)$$

Interestingly, instead of relying on the conventional bulk-edge correspondence, the existence of $\mathcal{PT}$ edge states can be judged by evaluating the position of their EPs. The presence of EPs ensures the edge bands forming loops and crossing the

bulk band gap by going through these EPs, and the absence of EPs indicates that $\mathcal{PT}$ edge states are either absent or gapped out from complex-valued bulk bands. Using the condition $0 \leqslant g_k^2 \leqslant 4$, we find that the EPs stay near the Dirac points

TABLE I. Comparison between P-symmetric and $\mathcal{PT}$ symmetric edge states for two types of domain walls.

	P-symmetric	P-broken, $\mathcal{PT}$ symmetric
Locally P-broken domain wall	Valley edge states	$\mathcal{PT}$ edge states for *small* gain/loss
Locally P-symmetric domain wall		$\mathcal{PT}$ edge states for *arbitrary* gain/loss

if $r = 0$, $m_i \to 0$. In other words, the $\mathcal{PT}$ symmetry of the modes near the Dirac points is most easily broken compared to modes at other k in the Brillouin zone. This is generally true for bulk modes of the zigzag cut structure because the imaginary part of the complex bulk frequency abruptly changes at the Dirac points due to the perturbation of gain/loss. For a locally P-symmetric domain wall, if m_r is fixed and m_i is continuously increased from 0, the $\mathcal{PT}$ edge states first form two separate continuous dispersion curves along the k_x direction, then the EPs of edge states appear at $k_x = 0$ or 2π, which divide the edge states into $\mathcal{PT}$ edge states and the complex-valued edge states regimes, and move toward $k_x = \frac{2\pi}{3}$ and $\frac{4\pi}{3}$ and two edge state dispersion curves form a loop during this transition. In the second regime, edge states have parabolic dispersion curves and link the edge bands with bulk bands. Before reaching the Dirac point, the EPs recede back to $k_x = 0$ and 2π, and completely vanish after m_i is tuned to make $(r^2 + 1)(m_i + 1) > 4$. This phase transition in the position of the EPs is shown in Fig. 6(a). In the light red shaded area, no EPs exist, but the $\mathcal{PT}$ edge states at $k = \pi$ do, indicating only first regime exists. Therefore these edge states are continuous along k_x and gapped at $k_x = 0$, 2π, and the bulk and $\mathcal{PT}$ edge bands are no longer connected

through parabolic edge bands [Figs. 2(a) and 2(d)]. For large enough values m_r, EPs are absent at any m_i, and the edge bands detach from the bulk bands completely and remain real-valued. In case of a locally P-broken wall, as shown in Fig. 1(b), if m_r is fixed and m_i is continuously increased from 0, the $\mathcal{PT}$ edge states have continuous dispersion curves along k_x, then the EPs appear at $k_x = 0$ and 2π and move toward $k_x = \pi$. If $m_i = 1$, the EPs merge at $k_x = \pi$, which indicates that the edge states have broken $\mathcal{PT}$ symmetry, as shown in Fig. 6(b). In fact, complex dispersion of edge states is linear and 'degenerate' at $k_x = \pi$. If $m_i > 1$, the $\mathcal{PT}$ edge states completely vanish and only the second regime exists, corresponding to the light blue region in Fig. 6(b). This is consistent with the absence of $\mathcal{PT}$ edge states shown at the locally P-broken domain wall in Figs. 2(c) and 2(d).

We have also investigated the $\mathcal{PT}$ symmetric interfaces formed by other cuts, like bearded and armchair cuts, as shown in Figs. 1(c) and 1(d). The $\mathcal{PT}$ edge states are expected to exist in these configurations as well due to the $\mathcal{PT}$ symmetry of Hamiltonian. The study of these cases is summarized in Ref. [48]. For the bearded cut, the positions of the EPs for locally P-symmetric and locally P-broken domain walls are given by

$$g_k = \begin{cases} \pm\frac{1}{2}\left(m_i - \sqrt{m_i^2 + \frac{4}{r^2+1}}\right), & \text{locally P} - \text{symmetric domain wall}, \\ \pm\frac{1}{2}\left(m_i + \sqrt{m_i^2 + \frac{4}{r^2+1}}\right), & \text{locally P} - \text{broken domain wall}. \end{cases} \tag{22}$$

For a locally P-symmetric domain wall, the EPs move in k_x between $\pm(\frac{2\pi}{3}, \pi)$ [Fig. 6(c)] and never vanish since $0 < |g_k| < 1$ as long as $m_i \neq 0$. Thus the loop-shaped dispersion curves of $\mathcal{PT}$ edge states located at the locally P-symmetric domain wall always exist, and are robust against the perturbation of both the real and imaginary part of onsite potential. For a locally P-broken domain wall, the EPs exist between wave number $\pm(0, \pi)$ and disappear if m_i is large enough to make $|g_k| > 1$ [Fig. 6(d)]. Note that the decay length κ^{-1} of the $\mathcal{PT}$ edge states for the bearded cut keeps approaching zero within a larger range in k_x if m_i increases, and it is smaller on average than that for the zigzag cut. $\mathcal{PT}$ symmetric interfaces for armchair cuts, however, always have two $\mathcal{PT}$ edge loops or four gapped $\mathcal{PT}$ edge bands that are doubly degenerate in energy, since there is no parity difference between the inner and the outer domain walls. The above analysis indicates that the robustness of $\mathcal{PT}$ edge states against the magnitude of gain/loss is a special feature of the honeycomb lattice, although $\mathcal{PT}$ edge states might exist in other lattice structures with $\mathcal{PT}$ symmetric interfaces.

Our analysis also clearly demonstrates the importance of the local P symmetry of the domain wall for the system

with gain/loss; this symmetry enforces the presence of edge states, and prevents the breaking of global $\mathcal{PT}$ symmetry. The comparison between the valley edge states and $\mathcal{PT}$-edge states for both domain wall configurations is summarized in Table I.

Other configurations of gain and loss crystals without $\mathcal{PT}$ symmetric interface, schematized in Fig. S4, do not support lossless edge states. Hamiltonians constructed from these configurations are not $\mathcal{PT}$-invariant. Details for different non-$\mathcal{PT}$ symmetric interfaces are explained in Ref. [48].

VI. NON-HERMITIAN HALDANE MODEL

The second type of NH model we consider is a Haldane honeycomb lattice consisting of two domains with zigzag cuts at the ends of the strip [53]. Next-nearest-neighbor (NNN) complex hopping is considered with amplitude t' and phase factor $e^{-i\Phi}$ corresponding to the Haldane flux. In order to construct the $\mathcal{PT}$ symmetric interface, we introduce gain at the A sites in domain I, and loss at the B sites in domain II. Periodic boundary conditions are applied along the direction x_1 and open boundary conditions are applied at the ends of

TABLE II. Complex frequency correction $\delta\Omega_0$ and mass term m in the effective Hamiltonian due to gain, loss, and inversion symmetry breaking. $M, M' \propto \Delta$.

	$\epsilon_A = \epsilon_1 - i\Delta, \epsilon_B = \epsilon_1$	$\epsilon_A = \epsilon_1 + i\Delta, \epsilon_B = \epsilon_1$	$\epsilon_A = \epsilon_1, \epsilon_B = \epsilon_1 - i\Delta$	$\epsilon_A = \epsilon_1, \epsilon_B = \epsilon_1 + i\Delta$
m	$(\frac{\Delta}{\epsilon_1} - i)M$	$(\frac{\Delta}{\epsilon_1} + i)M$	$(\frac{-\Delta}{\epsilon_1} + i)M$	$-(i + \frac{\Delta}{\epsilon_1})M$
$\delta\Omega_0$	$(\frac{\Delta}{\epsilon_1} + i)M'$	$(\frac{\Delta}{\epsilon_1} - i)M'$	$(\frac{\Delta}{\epsilon_1} + i)M'$	$(\frac{\Delta}{\epsilon_1} - i)M'$

strip along x_2 (Fig. 5). If the magnetic fluxes in domain I and II have the same distribution [Fig. 5(a)], then the $\mathcal{PT}$ symmetry along the domain wall is destroyed by the local magnetic flux. The $\mathcal{PT}$ symmetry of the interface can be restored by switching the direction of magnetic fluxes in either one of the domains, as seen in Fig. 5(b). The equations of motion for the two configurations are

$$\epsilon\psi_{I,A}(n) = -h_+\psi_{I,A}(n) - g_-(\psi_{I,A}(n+1) + \psi_{I,A}(n-1)) - \psi_{I,B}(n+1) - g_0\psi_{I,B}(n) - im_i\psi_{I,A}(n),$$
$$\epsilon\psi_{I,B}(n) = -h_-\psi_{I,B}(n) - g_+(\psi_{I,B}(n+1) + \psi_{I,B}(n-1)) - \psi_{I,A}(n-1) - g_0\psi_{I,A}(n);$$
$$\epsilon\psi_{II,A}(n) = -h_\pm\psi_{II,A}(n) - g_\mp(\psi_{II,A}(n+1) + \psi_{II,A}(n-1)) - \psi_{II,B}(n-1) - g_0\psi_{II,B}(n),$$
$$\epsilon\psi_{II,B}(n) = -h_\mp\psi_{II,B}(n) - g_\pm(\psi_{II,B}(n+1) + \psi_{II,B}(n-1)) - \psi_{II,A}(n+1) - g_0\psi_{II,A}(n) + im_i\psi_{I,A}(n),$$
$$n = 1, 2, \ldots, N-1, \tag{23}$$

where $h_\pm = 2t'\cos(k \pm \Phi)$, $g_\pm = 2t'\cos(k/2 \pm \Phi)$, and $g_0 = 2\cos(\frac{k}{2})$. The magnetic fluxes are not present at the domain wall, thus the boundary conditions are

$$\epsilon\psi_{I,A}(0) = -h_+\psi_{I,A}(0) - g_-(\psi_{I,A}(1) + \psi_{II,A}(0)) - \psi_{I,B}(1) - g_0\psi_{I,B}(0) + m\psi_{I,A}(0),$$
$$\epsilon\psi_{I,B}(0) = -h_-\psi_{I,B}(0) - g_+(\psi_{I,B}(1) + \psi_{II,B}(0)) - \psi_{II,A}(0) - g_0\psi_{I,A}(0),$$
$$\epsilon\psi_{II,A}(0) = -h_\pm\psi_{II,A}(0) - g_\mp(\psi_{II,A}(1) + \psi_{I,A}(0)) - \psi_{I,B}(0) - g_0\psi_{II,B}(0),$$
$$\epsilon\psi_{II,B}(0) = -h_\mp\psi_{II,B}(0) - g_\pm(\psi_{II,B}(1) + \psi_{I,B}(0)) - \psi_{II,A}(1) - g_0\psi_{II,A}(0) + m^*\psi_{I,A}(0), \tag{24}$$

where $m = im_i$. From the previous analysis, we predict that the $\mathcal{PT}$ edge states localized at the domain wall cannot exist in the first configuration shown in Fig. 7(a), but might be present in the second configuration shown in Fig. 7(b) as long as the $\mathcal{PT}$ symmetry of the edge states is preserved. The bulk topological invariant of the Haldane model is not changed by introducing the gain/loss into the system without closing the bulk band gap, though Berry connection is redefined in the context of NH system. The completeness and orthogonality conditions are only satisfied in the biorthogonal basis [34],

and correspondingly the Chern number is defined as

$$c = c^{\zeta,\eta} = c^{\eta,\zeta}, \zeta, \quad \eta = R, L, \quad \zeta \neq \eta, \tag{25}$$

where the subscript denotes the right/left basis. It can be shown that the Chern number in Eq. (25) is uniquely defined and is quantized the same way as in the Hermitian context. The details of the gauge transformation and derivation of Berry connection for the NH Haldane model are given in Ref. [48]. Based on the bulk-interface correspondence, we predict that topological edge states will be present and localized at the ends of the strip and at the domain wall even though their energies might be complex valued, as long as the bulk band gap is not closed.

These predictions are verified by the TBM, and the complex band structures for two configurations are shown in Fig. 8. In both cases, all the edge bands are connected with the bulk bands. One-way propagation is also observed for the edge states, revealing the nonreciprocal (chiral) nature of topological edge states in the Haldane model. In the second configuration, edge states localized at the $\mathcal{PT}$ symmetric interface have two regimes as well, namely, $\mathcal{PT}$ symmetry preserved regime and $\mathcal{PT}$ symmetry spontaneously broken regime, and these regimes are connected by the EPs. The edge states bridge the gapped bulk bands in both directions of real and imaginary energies through the two parabolic edge bands [Fig. 8(b)], while the edge states discussed in the valley case bridge the gapped bulk bands only in the direction of imaginary energy. If the magnitude of gain/loss is
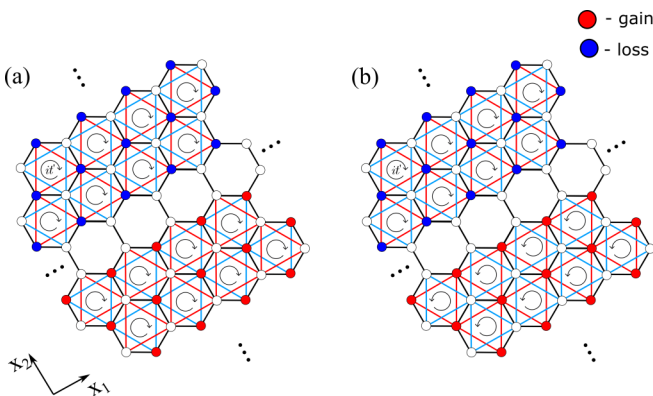

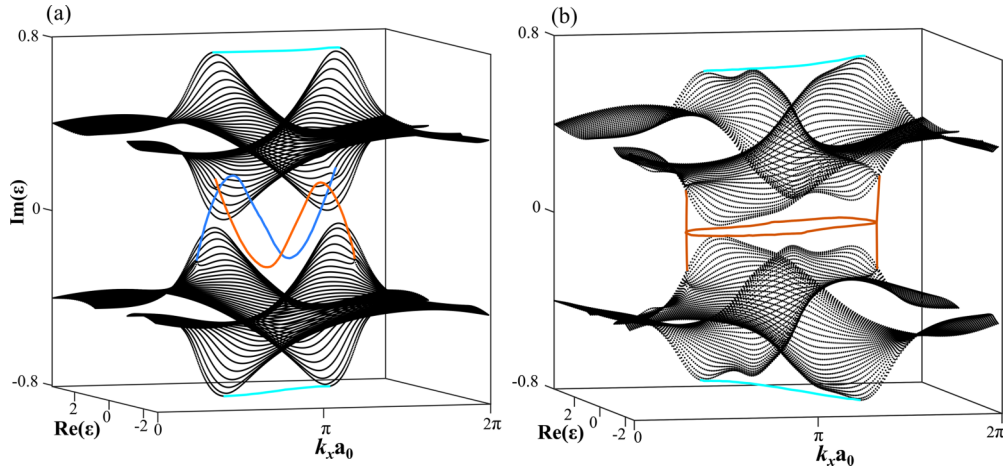FIG. 7. Schematics of non-Hermitian Haldane model without (a) and with (b) the $\mathcal{PT}$ symmetric interface.

FIG. 8. Complex band structures with $m_i = 0.8$, $t' = 0.2$,(a) $\phi = \frac{\pi}{3}$ for both domains (b) $\phi = \frac{\pi}{3}$ in the domain I and $\phi = -\frac{\pi}{3}$ in domain II. The cyan curves show the topological edge states located at the ends of the strip, and the red and blue bands in (a) are topological edge states at the domain wall, while the red loop bands in (b) are the topological $\mathcal{PT}$ edge states following from topological bulk invariance. The number of unit cells for each domain is $N = 60$.

very large, the bulk bands above and below $\mathcal{PT}$ edge states in the imaginary energy direction merge with each other, causing the disappearance of topological edge states localized at the ends of chain, while edge states at the interface of two domains always survive. Hence the robustness of $\mathcal{PT}$ symmetry is demonstrated by the fact that topological edge states at the ends of chain vanish but edge states located at the $\mathcal{PT}$ symmetric interface survive beyond the critical value of gain and loss.

VII. OPTICAL IMPLEMENTATION OF $\mathcal{PT}$ SYMMETRIC INTERFACES IN PHOTONIC GRAPHENE

$\mathcal{PT}$ symmetric systems can be realized in various settings including optical lattices, coupled waveguides, microresonators, and metamaterials [54–60]. To confirm our analytical prediction of $\mathcal{PT}$ edge states in the first regime, we now consider an electromagnetic model relevant to photonics. Specifically, we emulate $\mathcal{PT}$ symmetric interfaces in 2D honeycomb photonic crystals composed of dielectric rods (photonic graphene) with the imaginary corrections introduced to the dielectric permittivities of the rods, $\text{Im}(\epsilon_A) = \Delta$ at sites A in domain I and $\text{Im}(\epsilon_B) = -\Delta$ at sites B in domain II.

The effective photonic Hamiltonian near the Dirac points for the photonic crystal with the gain/loss introduced at one site of the unit cell is derived by using the plane-wave expansion of Maxwell's equations (Ref. [48])

$$\hat{H}_{K(K')} = \Omega_0 + \delta\Omega_0 \pm V\delta k_x \hat{\sigma}_x + V\delta k_y \hat{\sigma}_y + m\hat{\sigma}_z, \quad (26)$$

where $\Omega_0 = K^2(\tilde{\epsilon}_0 + \tilde{\epsilon}_1)$ stands for the unperturbed onsite frequency, $\delta\Omega_0$ denotes the complex correction of the onsite energy, m is the complex mass term due to gain/loss of the material, and $V = K(\tilde{\epsilon}_0 + \tilde{\epsilon}_1)$ is the Fermi velocity. We list the values of m and $\delta\Omega_0$ for different configurations of the unit cell in Table II. Among them, the crystals $\epsilon_A = \epsilon_1 \mp i\Delta$, $\epsilon_B = \epsilon_1$ and $\epsilon_A = \epsilon_1$, $\epsilon_B = \epsilon_1 \pm i\Delta$ are $\mathcal{PT}$ symmetric partners.

As follows from Eq. (26), the band degeneracy at the Dirac point is slightly lifted due to the real part of the mass term m_r being of order Δ^2 and inducing inversion symmetry breaking in the unit cell. Moreover, the bulk bands become flattened near the Dirac point due to the imaginary part $m_i \propto \Delta$. These peculiar properties, not observed in Hermitian systems, are confirmed by both tight-binding and plane-wave expansion calculations (Fig. S7). Therefore photonic lattices with a $\mathcal{PT}$ symmetric interface exhibit an effective onsite perturbed potential $\propto \Delta^2$ at sites A in domain I and at sites B in domain II. This corresponds to the model discussed in Sec. II with $m_r < m_i$ [see Fig. 2(c)]. To model the non-$\mathcal{PT}$ symmetric interface, we build the structure in such a way that $\text{Im}(\epsilon_A) = \Delta$ in domain I and $\text{Im}(\epsilon_A) = -\Delta$ in domain II, which corresponds to the third configuration discussed in Supplemental Material V in Ref. [48].

While the effective kp Hamiltonian (26) accurately describes the bulk dispersion in the vicinity of the Dirac points, it requires corrections that are quadratic in δk to reproduce the dispersion of the $\mathcal{PT}$ edge states. This is in obvious contrast to the valley edge states, which are captured already by a linear-in-δk Hamiltonian. In Ref. [48], we present a rigorous derivation of the effective $\boldsymbol{k \cdot p}$ Hamiltonian with δk^2 terms from the tight-binding method and establish the correspondence between $\boldsymbol{k \cdot p}$ and tight-binding considerations of $\mathcal{PT}$ and valley edge states near the Dirac point, discussed in Sec. II. The δk^2 corrections to the Hamiltonian (26) can be straightforwardly derived from the plane-wave expansion in the same fashion.

The full-wave simulations of electromagnetic response of the photonic crystal supercells with different cuts at the interfaces (zigzag, bearded, and armchair) are performed using a finite-element method (FEM) solver (COMSOL Multiphysics). Periodic boundary conditions are imposed in $x_1 = (1, 0)$ and $x_2 = (\frac{1}{2}, \frac{\sqrt{3}}{2})$ directions of the supercell, with domains I and II in the lower and upper regions, respectively (Fig. 9, left panel). Thereby, two $\mathcal{PT}$ symmetric interfaces are simultaneously present in the geometry. Results of first-principles simulations are summarized in Fig. 9.
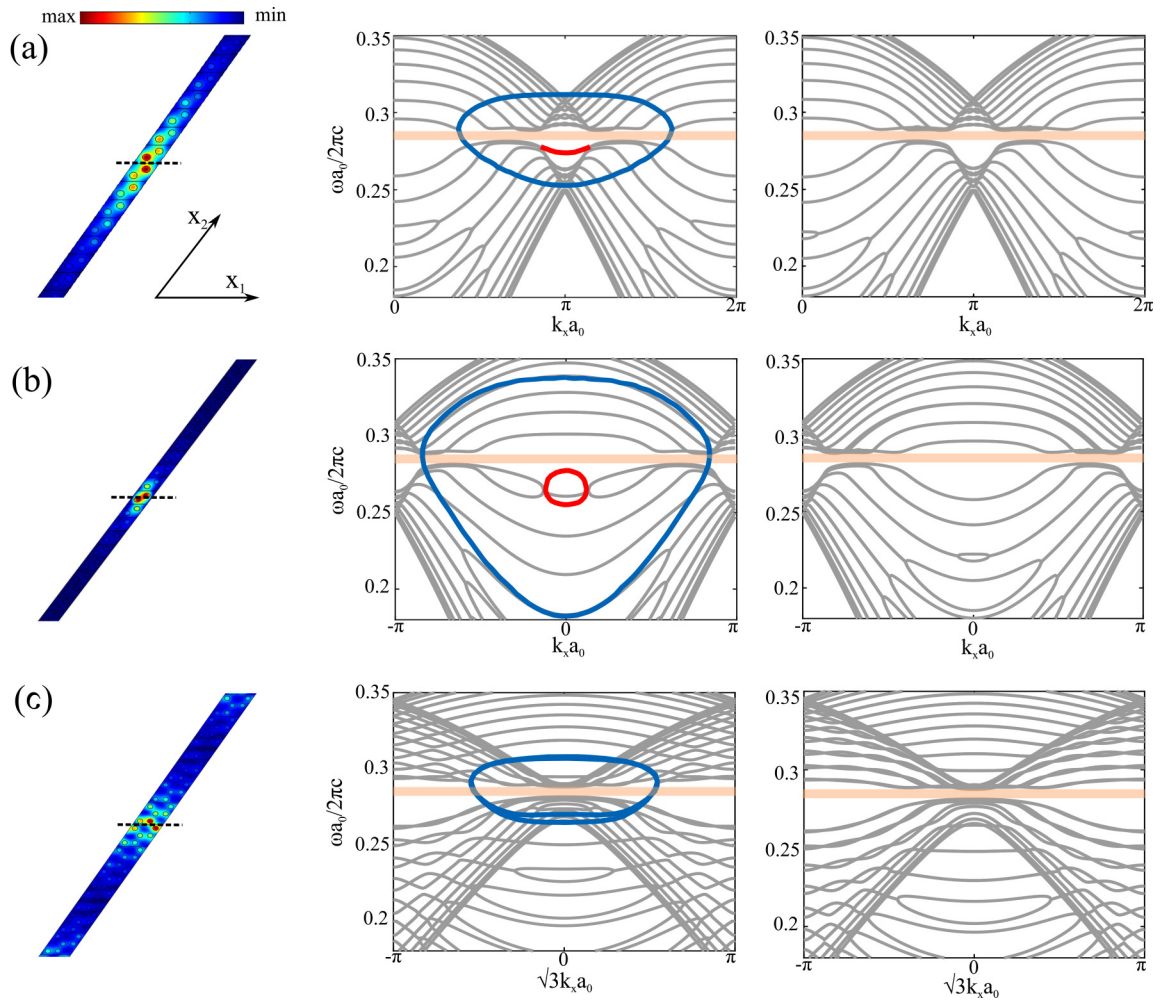
FIG. 9. Optical implementation of $\mathcal{PT}$ interfaces in photonic graphene with different cuts at the interfaces (indicated by black dash line): (a) zigzag, (b) bearded, and (c) armchair shaped boundaries. (Left) Normal electric field $|E|$ profiles for the edge modes localized at different cuts of interfaces between photonic crystals with gain and loss. Middle panels: dispersion (the real part of frequency) for $\mathcal{PT}$ symmetric domain walls. Right panels: dispersion for non-$\mathcal{PT}$ domain walls. Branches of $\mathcal{PT}$ edge states located at locally parity-symmetric and parity-broken interfaces are shown in blue and red, respectively, and bands of dissipative bulk modes in grey. The band gap is indicated by a pink shaded region. The crystals are made of dielectric rods of radius $r_a = r_b = 0.15a_0$ with permittivity $\epsilon_1 = 14$ and gain/loss parameter $\Delta = 5$ embedded in air.

First, we model $\mathcal{PT}$ and non-$\mathcal{PT}$ interfaces with zigzag cuts at the boundaries. In the middle panel of Fig. 9(a) the lossless loop bands (blue color) centered at $k_x = \pi/a_0$ are observed, and these $\mathcal{PT}$ edge states are localized at the locally P-symmetric domain wall only, as shown in the left panel. The magnitude of gain/loss Δ is chosen large enough to make EPs of the $\mathcal{PT}$ edge states located at the locally P-broken domain wall disappear, but not large enough to separate the loop bands for $\mathcal{PT}$ edge states located at locally P-symmetric domain wall.

Second, for the bearded locally P-symmetric and locally P-broken interfaces, $\mathcal{PT}$ edge states with large and small loop bands are observed centered at $k_x = 0$, as seen in Fig. 9(b). We notice that the edge modes at the bearded cut generally decay faster away from the domain wall than those at the zigzag cut. This property is mentioned in Sec. II and discussed in detail in Ref. [48].

Third, two lossless loop bands are found at the armchair $\mathcal{PT}$ interfaces and localized at both the domain walls, since

the domain walls in this geometry locally have no parity difference.

For all three non-$\mathcal{PT}$ symmetric interfaces, no $\mathcal{PT}$ edge states in the band gaps of bulk modes are found, as seen in the right panel of Fig. 9. Thus our numerical results are consistent with the tight-binding calculations and analytical predictions.

VIII. CONCLUSIONS

In this paper, we have demonstrated that $\mathcal{PT}$ symmetric interfaces between domains of non-Hermitian lattices with "gain" and "loss" support edge states which exhibit $\mathcal{PT}$ phase transitions. Two model systems, based on valley insulator and Chern insulator models, are investigated. For the valley-Hall insulator, a rigorous symmetry analysis comparing the conventional (Hermitian) valley edge states and the edge states of the $\mathcal{PT}$ symmetric structure is presented. We found that if the local parity symmetry at the domain wall is broken,

the $\mathcal{PT}$ edge states preserving the $\mathcal{PT}$ symmetric phase exist only for certain values of the gain/loss parameters, underlining the important role of spatial symmetries at the interface for the valley Hall systems. The existence of these edge states is linked to EPs in the edge band; by tuning the magnitude of the gain/loss, it is possible to annihilate the EPs, so that the $\mathcal{PT}$ symmetry is spontaneously broken and the edge spectrum becomes complex-valued. If the domain wall is locally parity-symmetric, the $\mathcal{PT}$ edge states are always present no matter how the system is perturbed by an onsite potential or gain/loss.

To further explore the interplay of non-Hermiticity and topology, we studied the non-Hermitian Haldane model and demonstrated the robustness of its topological features to the introduction of gain/loss. We found the one-way edge states localized to the $\mathcal{PT}$ symmetric interfaces that also exhibit $\mathcal{PT}$ phase transition and interconnect bulk bands by branching out into the imaginary energy dimension. Since these edge states are strong in a topological sense (as opposed to the valley states), they persist for large magnitudes of gain/loss, as long as bulk states are gapped.

Last but not least, experimentally feasible optical analogs of honeycomb lattices with and without $\mathcal{PT}$ symmetric interface have been studied using first-principles numerical methods, which confirmed the analytical predictions. This work envisions a generalization of Hermitian topological edge states into the NH topological edge states which exhibits a $\mathcal{PT}$ phase transition.

[1] M. Z. Hasan and C. L. Kane, Rev. Mod. Phys. **82**, 3045 (2010).

[2] X. L. Qi and S. C. Zhang, Rev. Mod. Phys. **83**, 1057 (2011).

[3] B. A. Bernevig and T. L. Hughes, *Topological Insulators and Topological Superconductors* (Princeton University Press, Princeton, 2013).

[4] C. L. Kane and E. J. Mele, Phys. Rev. Lett. **95**, 226801 (2005).

[5] C. L. Kane and E. J. Mele, Phys. Rev. Lett. **95**, 146802 (2005).

[6] B. A. Bernevig, T. L. Hughes, and S. C. Zhang, Science **314**, 1757 (2006).

[7] B. A. Bernevig and S. C. Zhang, Phys. Rev. Lett. **96**, 106802 (2006).

[8] F. D. M. Haldane and S. Raghu, Phys. Rev. Lett. **100**, 013904 (2008).

[9] S. Raghu and F. D. M. Haldane, Phys. Rev. A **78**, 033834 (2008).

[10] Z. Wang, Y. D. Chong, J. D. Joannopoulos, and M. Soljacic, Nature (London) **461**, 772 (2009).

[11] L. Feng, M. Ayache, J. Q. Huang, Y. L. Xu, M. H. Lu, Y. F. Chen, Y. Fainman, and A. Scherer, Science **333**, 729 (2011).

[12] M. Hafezi, E. A. Demler, M. D. Lukin, and J. M. Taylor, Nat. Phys. **7**, 907 (2011).

[13] K. J. Fang, Z. F. Yu, and S. H. Fan, Nat. Photonics **6**, 782 (2012).

[14] A. B. Khanikaev, S. H. Mousavi, W. K. Tse, M. Kargarian, A. H. MacDonald, and G. Shvets, Nat. Mater. **12**, 233 (2013).

[15] M. C. Rechtsman, J. M. Zeuner, Y. Plotnik, Y. Lumer, D. Podolsky, F. Dreisow, S. Nolte, M. Segev, and A. Szameit, Nature (London) **496**, 196 (2013).

[16] R. Susstrunk and S. D. Huber, Proc. Natl. Acad. Sci. USA **113**, E4767 (2016).

[17] V. Peano, C. Brendel, M. Schmidt, and F. Marquardt, Phys. Rev. X **5**, 031011 (2015).

[18] Z. J. Yang, F. Gao, X. H. Shi, X. Lin, Z. Gao, Y. D. Chong, and B. L. Zhang, Phys. Rev. Lett. **114**, 114301 (2015).

[19] S. D. Huber, Nat. Phys. **12**, 621 (2016).

[20] X. J. Cheng, C. Jouvaud, X. Ni, S. H. Mousavi, A. Z. Genack, and A. B. Khanikaev, Nat. Mater. **15**, 542 (2016).

[21] L. A. Fu, Phys. Rev. Lett. **106**, 106802 (2011).

[22] G. W. Semenoff, V. Semenoff, and F. Zhou, Phys. Rev. Lett. **101**, 087204 (2008).

[23] S. A. Skirlo, L. Lu, and M. Soljacic, Phys. Rev. Lett. **113**, 113904 (2014).

[24] S. A. Skirlo, L. Lu, Y. C. Igarashi, Q. H. Yan, J. Joannopoulos, and M. Soljacic, Phys. Rev. Lett. **115**, 253901 (2015).

[25] L. Feng, R. E. Ganainy, and L. Ge, Nat. Photonics **11**, 752 (2017).

[26] R. El-Ganainy, K. G. Makris, M. Khajavikhan, Z. H. Musslimani, S. Rotter, and D. N. Christodoulides, Nat. Phys. **14**, 11 (2018).

[27] Y. C. Hu and T. L. Hughes, Phys. Rev. B **84**, 153101 (2011).

[28] M. S. Rudner and L. S. Levitov, Phys. Rev. Lett. **102**, 065703 (2009).

[29] K. Esaki, M. Sato, K. Hasebe, and M. Kohmoto, Phys. Rev. B **84**, 205128 (2011).

[30] H. Schomerus, Opt. Lett. **38**, 1912 (2013).

[31] J. M. Zeuner, M. C. Rechtsman, Y. Plotnik, Y. Lumer, S. Nolte, M. S. Rudner, M. Segev, and A. Szameit, Phys. Rev. Lett. **115**, 040402 (2015).

[32] T. E. Lee, Phys. Rev. Lett. **116**, 133903 (2016).

[33] D. Leykam, K. Y. Bliokh, C. L. Huang, Y. D. Chong, and F. Nori, Phys. Rev. Lett. **118**, 040401 (2017).

[34] H. T. Shen, B. Zhen, and L. Fu, Phys. Rev. Lett. **120**, 146402 (2018).

[35] S. Weimann, M. Kremer, Y. Plotnik, Y. Lumer, S. Nolte, K. G. Makris, M. Segev, M. C. Rechtsman, and A. Szameit, Nat. Mater. **16**, 433 (2017).

[36] G. Q. Liang and Y. D. Chong, Phys. Rev. Lett. **110**, 203904 (2013).

[37] G. Harari, Y. Plotnik, M. A. Bandres, Y. Lumer, M. Rechtsman, and M. Segev, CLEO: QELS_Fundamental Science 2015 (2015).

[38] C. M. Bender and S. Boettcher, Phys. Rev. Lett. **80**, 5243 (1998).

[39] P. Dorey, C. Dunning, and R. Tateo, J. Phys. A **34**, 5679 (2001).

[40] C. M. Bender, D. C. Brody, and H. F. Jones, Phys. Rev. Lett. **89**, 270401 (2002).

[41] A. Mostafazadeh, J. Math. Phys. **43**, 2814 (2002).

[42] M. V. Berry, Czech J. Phys. **54**, 1039 (2004).

[43] W. D. Heiss, J. Phys. A **37**, 2455 (2004).

[44] W. D. Heiss, J. Phys. A **45**, 444016 (2012).

[45] B. Bahari, A. Ndao, F. Vallini, A. El Amili, Y. Fainman, and B. Kante, Science **358**, 636 (2017).

[46] M. A. Bandres, S. Wittek, G. Harari, M. Parto, J. Ren, M. Segev, D. N. Christodoulides, and M. Khajavikhan, Science **359**, eaar4005 (2018).

[47] G. Harari, M. A. Bandres, Y. Lumer, M. C. Rechtsman, Y. D. Chong, M. Khajavikhan, D. N. Christodoulides, and M. Segev, Science **359**, eaar4003 (2018).

[48] See Supplemental Material at http://link.aps.org/supplemental/10.1103/PhysRevB.98.165129 for discussion of several aspects in detail related to the $\mathcal{PT}$ edge states and non-Hermitian system, which include; I. tight-binding description of the lattice model; II. the analysis of decay lengths for the dissipationless edge states located at the $\mathcal{PT}$ symmetric interface formed by zigzag edge; III. detailed derivation of the $\mathbf{k} \cdot \mathbf{p}$ method applied for the $\mathcal{PT}$ edge states; IV. the discussion of $\mathcal{PT}$ edge states in other types of interfaces like bearded and armchair edges; V. the proof of non-existence of $\mathcal{PT}$ edge states in the non-$\mathcal{PT}$ symmetric interfaces; VI. the discussion of Chern number in the non-Hermitian Haldane model; VII. the exhaustive derivation of effective non-Hermitian electromagnetic Hamiltonian for honeycomb photonic lattice with gain/loss introduced.

[49] A. H. Castro Neto, F. Guinea, N. M. R. Peres, K. S. Novoselov, and A. K. Geim, Rev. Mod. Phys. **81**, 109 (2009).

[50] D. Xiao, W. Yao, and Q. Niu, Phys. Rev. Lett. **99**, 236809 (2007).

[51] H. Schomerus and J. Wiersig, Phys. Rev. A **90**, 053819 (2014).

[52] D. C. Brody, J. Phys. A **47**, 035305 (2014).

[53] F. D. M. Haldane, Phys. Rev. Lett. **61**, 2015 (1988).

[54] A. Guo, G. J. Salamo, D. Duchesne, R. Morandotti, M. Volatier-Ravat, V. Aimez, G. A. Siviloglou, and D. N. Christodoulides, Phys. Rev. Lett. **103**, 093902 (2009).

[55] L. Feng, Y. L. Xu, W. S. Fegadolli, M. H. Lu, J. E. B. Oliveira, V. R. Almeida, Y. F. Chen, and A. Scherer, Nat. Mater. **12**, 108 (2013).

[56] L. Feng, Z. J. Wong, R. M. Ma, Y. Wang, and X. Zhang, Science **346**, 972 (2014).

[57] M. Lawrence, N. N. Xu, X. Q. Zhang, L. Q. Cong, J. G. Han, W. L. Zhang, and S. Zhang, Phys. Rev. Lett. **113**, 093901 (2014).

[58] B. Peng *et al.*, Nat. Phys. **10**, 394 (2014).

[59] J. S. Tang *et al.*, Nat. Photonics **10**, 642 (2016).

[60] Y. L. Xu, W. S. Fegadolli, L. Gan, M. H. Lu, X. P. Liu, Z. Y. Li, A. Scherer, and Y. F. Chen, Nat. Commun. **7**, 11319 (2016).